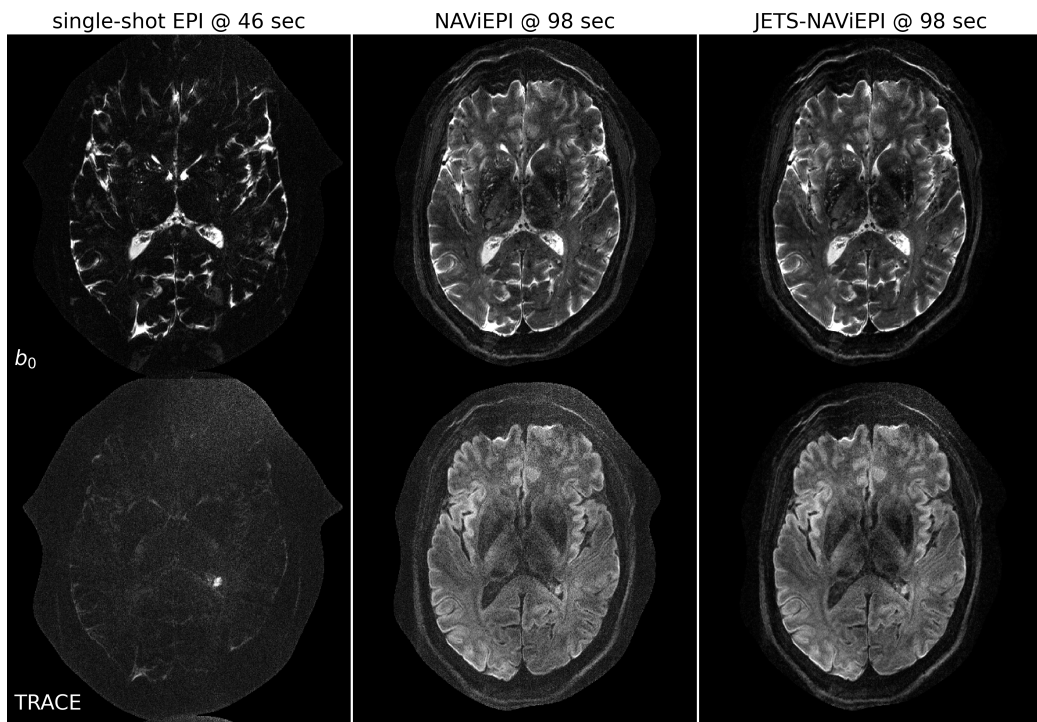


Graphical Abstract

Accelerated Diffusion Weighted Magnetic Resonance Imaging at 7 T: Joint Reconstruction for Shift-Encoded Navigator-based Interleaved Echo Planar Imaging (JETS-NAViEPI)

Zhengguo Tan, Patrick Alexander Liebig, Robin Martin Heidemann, Frederik Bernd Laun, Florian Knoll

3-scan trace acquisition with voxel size 0.5 X 0.5 X 2.0 mm³



Highlights

Accelerated Diffusion Weighted Magnetic Resonance Imaging at 7 T: Joint Reconstruction for Shift-Encoded Navigator-based Interleaved Echo Planar Imaging (JETS-NAViEPI)

Zhengguo Tan, Patrick Alexander Liebig, Robin Martin Heidemann, Frederik Bernd Laun, Florian Knoll

- Navigator-based interleaved EPI acquisition with minimal distortion mismatch between echoes
- Novel accelerated diffusion acquisition with shifted phase encoding among diffusion directions for complementary k - q -space sampling at 7 T
- Generalized joint k - q -slice diffusion-weighted image reconstruction with overlapping locally low-rank regularization
- Efficient simultaneous multi-slice (SMS) image reconstruction
- 3-scan trace acquisition with the voxel size $0.5 \times 0.5 \times 2.0 \text{ mm}^3$ and 60 slices at 1.5 min

Accelerated Diffusion Weighted Magnetic Resonance Imaging at 7 T: Joint Reconstruction for Shift-Encoded Navigator-based Interleaved Echo Planar Imaging (JETS-NAViEPI)

Zhengguo Tan^a, Patrick Alexander Liebig^b, Robin Martin Heidemann^b,
Frederik Bernd Laun^c, Florian Knoll^a

^a*Department Artificial Intelligence in Biomedical Engineering (AIBE),
Friedrich-Alexander University of Erlangen-Nuremberg, Erlangen, Germany*

^b*Siemens Healthcare GmbH, Erlangen, Germany*

^c*Institute of Radiology, University Hospital Erlangen, Friedrich-Alexander University of Erlangen-Nuremberg, Erlangen, Germany*

Abstract

The pursuit of high spatial-angular-temporal resolution for in vivo diffusion-weighted magnetic resonance imaging (DW-MRI) at ultra-high field strength (7 T and above) is important in understanding brain microstructure and function. Such pursuit, however, faces several technical challenges. First, increased off-resonance and shorter T_2 relaxation require faster echo train readouts. Second, existing high-resolution DW-MRI techniques usually employ in-plane fully-sampled multi-shot EPI, which not only prolongs the scan time but also induces a high specific absorption rate (SAR) at 7 T. To address these challenges, we develop in this work navigator-based interleaved EPI (NAViEPI) which enforces the same effective echo spacing (ESP) between the imaging and the navigator echo. First, NAViEPI renders no distortion mismatch between the two echoes, and thus simplifies shot-to-shot phase variation correction. Second, NAViEPI allows for a large number of shots

(e.g. > 4) with undersampled iEPI acquisition, thereby rendering clinically-feasible high-resolution sub-millimeter protocols. To retain signal-to-noise ratio (SNR) and to reduce undersampling artifacts, we developed a k_y -shift encoding among diffusion encodings to explore complementary k - q -space sampling. Moreover, we developed a novel joint reconstruction with overlapping locally low-rank regularization generalized to the multi-band multi-shot acquisition at 7 T (dubbed JETS-NAViEPI). Our method was demonstrated with experimental results covering 1 mm isotropic resolution multi b -value DWI and sub-millimeter in-plane resolution fast TRACE acquisition.

Keywords: Diffusion-weighted magnetic resonance imaging, Echo planar imaging, Navigator, Ultra-high field, Joint reconstruction, Low rank, Simultaneous multi slice

¹ **1. Introduction**

² Diffusion-weighted magnetic resonance imaging (DW-MRI) ([Le Bihan et al., 1986; Merboldt et al., 1985](#)) is a non-invasive modality that is sensi-
³ tive to the intravoxel Brownian motion of water molecules. DW-MRI forms
⁴ the basis for diffusion tensor imaging (DTI) ([Basser et al., 1994; Mori et al., 1999](#)) and high angular resolution diffusion imaging (HARDI) ([Tuch et al., 2002](#)), and has been widely used in acute brain ischemia diagnosis, in tumor
⁵ detection and staging, and in neuroscience ([Jones, 2010](#)).

⁶ For DW-MRI acquisition, the commonly used pulse sequence is single-
⁷ shot echo-planar imaging (SS-EPI) ([Mansfield, 1977](#)). SS-EPI is capable of
⁸ rapidly acquiring one DW image per radio-frequency excitation at the order
⁹ of 100 ms, and is thus motion robust. However, conventional SS-EPI, even
¹⁰ with three-fold accelerated acquisition ([Bammer et al., 2001](#)) using parallel
¹¹ imaging ([Roemer et al., 1990; Ra and Rim, 1993; Pruessmann et al., 1999](#);
¹² [Griswold et al., 2002](#)), still suffers from low spatial resolution and geometric
¹³ distortions.

¹⁴ In the quest for high spatial-angular-temporal-resolution and minimal-
¹⁵ geometry-distortion DW-MRI, tremendous efforts have been made. Tech-
¹⁶ niques for the correction of image distortions induced by off-resonances and
¹⁷ eddy currents have been developed ([Andersson et al., 2003](#)). Furthermore,
¹⁸ gSlider ([Setsompop et al., 2018](#)) with blipped-CAIPI ([Setsompop et al., 2012](#))
¹⁹ for simultaneous multi-slice (SMS) ([Maudsley, 1980; Breuer et al., 2005](#))
²⁰ was proposed to achieve high-resolution DW-MRI. Advanced pulse sequences
²¹ based on multi-shot EPI have also been developed, including but not limited
²² to interleaved EPI (iEPI) ([Butts et al., 1993](#)), PROPELLER ([Pipe et al., 2004](#)),

26 2002), and readout-segmented EPI (rsEPI) (Porter and Heidemann, 2009;
27 Heidemann et al., 2010).

28 Based on four-shot iEPI, multiplexed sensitivity encoding (MUSE) image
29 reconstruction achieved DW-MRI with a sub-millimeter in-plane resolution
30 and maximal b -value 800 s/mm^2 at 3 T (Chen et al., 2013). The four-shot
31 iEPI employed in MUSE acquired an in-plane fully-sampled k -space, except
32 partial Fourier. Every shot (segment), corresponding to four-fold under-
33 sampling, was then reconstructed via parallel imaging to obtain shot-to-shot
34 phase variation. This indicates that increasing the number of shots in MUSE
35 will result in higher undersampling per shot, and consequently, degrade shot
36 phase estimation (Wu and Miller, 2017).

37 Alternatively, navigator-based iEPI acquisition has been proposed (Jeong
38 et al., 2013; Dai et al., 2017, 2018). These proposals allow for a larger num-
39 ber of shots, and hence higher spatial resolution. However, due to the use of
40 different ESP between the imaging echo and the navigator echo, these pro-
41 posals suffered from geometric distortion mismatch between the two echoes
42 and thus required specific compensation methods. In contrast, rsEPI (Porter
43 and Heidemann, 2009; Heidemann et al., 2010) used the same readout seg-
44 ment for both echoes, and thus required no distortion correction of navigator
45 echoes.

46 Beyond the MUSE-type parallel imaging reconstruction, compressed sens-
47 ing (Lustig et al., 2007; Block et al., 2007) has been explored. For instance,
48 multi-shot reconstruction techniques based on structured low-rank matrix
49 completion (MUSSELS) (Mani et al., 2017; Bilgic et al., 2019) achieved 5-
50 shot DW-MRI with 9-fold undersampling per shot. Recently, JULEP (Dai

51 et al., 2023) incorporated explicit phase mapping into MUSSELS. These re-
52 construction techniques, i.e., MUSE, MUSSELS and JULEP, targeted the
53 reconstruction of one DW image from interleaved EPI acquisition, and did
54 not explore joint- k - q -space undersampling or reconstruction.

55 Joint- k - q -space undersampling can be achieved via proper regularization
56 along the diffusion encoding direction. Relevant examples are diffusion un-
57 dersampling with Gaussian process estimated reconstruction (DAGER) (Wu
58 et al., 2019) and magnitude-based spatial-angular locally low-rank regular-
59 ization (SPA-LLR) (Hu et al., 2020). However, DAGER addressed the re-
60 construction problem of single-shot EPI acquisition and SPA-LLR focused
61 on the reconstruction of single-band and fully-sampled iEPI acquisition.

62 In this work, we propose a Joint k - q -slice rEconsTruction framework
63 for Shift-encoded NAVigator-based interleaved EPI at 7 T (dubbed JETS-
64 NAViEPI). Our pulse sequence, NAViEPI, differs from most existing tech-
65 niques. First, NAViEPI builds upon interleaved EPI, thereby allowing for
66 fast and efficient k -space coverage. Second, inspired by rsEPI, NAViEPI en-
67 sures the same effective ESP between the imaging and the navigator echo,
68 thereby minimizing geometric distortion and allowing for the use of a larger
69 number of shots. NAViEPI essentially integrates the advantages of both iEPI
70 and rsEPI. Third, NAViEPI utilizes undersampled multi-shot iEPI, thereby
71 alleviating the SAR problem at 7 T. Fourth, NAViEPI shifts the k -space in-
72 plane sampling pattern along the phase encoding (k_y) direction. This shifting
73 creates complementary k - q -space sampling, which leads to the possibility of
74 our joint k - q -slice reconstruction. Specifically, we employ spatial-diffusion
75 overlapping LLR regularization to jointly reconstruct all diffusion encodings

⁷⁶ and multi-band slices. In vivo experiments at 7 T and comparisons with other
⁷⁷ techniques demonstrate the efficiency of our proposed method in achieving
⁷⁸ high spatial resolution DW-MRI at ultra-high field.

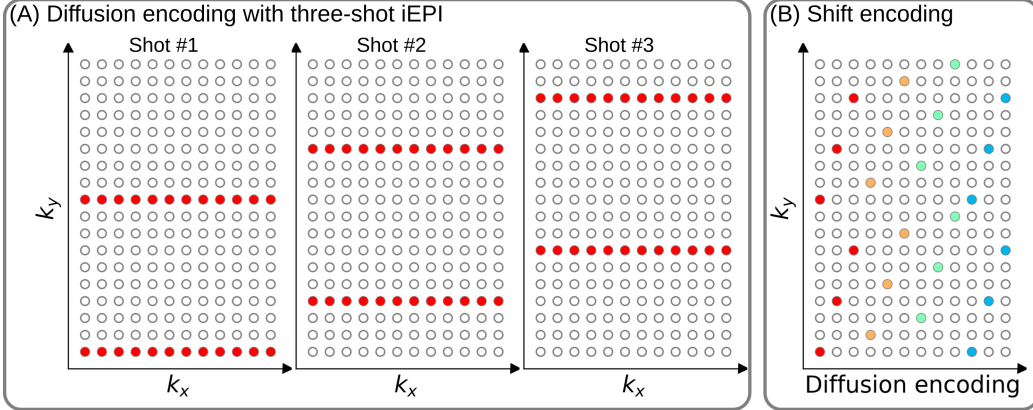


Figure 1: (A) An example DW-MRI acquisition with three-shot interleaved EPI acquisition. (B) The proposed k_y shifted diffusion encoding scheme. This example employs three shots per DW image. Therefore, every three columns have the same color.

79 2. Materials and methods

80 2.1. Multi-band shift-encoded iEPI acquisition

81 Fig. 1 (A) displays the diffusion-weighted image acquisition based on
 82 three-shot interleaved EPI with three-fold in-plane undersampling. Conven-
 83 tionally, such a sampling pattern is repeated for all diffusion directions. In
 84 contrast, we propose the k_y -shifted diffusion encoding, as shown in Fig. 1 (B).
 85 The interleaved EPI sampling pattern is shifted by one k_y line per diffusion
 86 direction, with the cycling period being the in-plane undersampling factor.

87 It is worth noting that, as shown in Fig. 1 (A), the undersampling factor
 88 of one segment is $R_{\text{in-plane}} \times N_{\text{shot}}$ (ignore multi-band undersampling here),
 89 yielding nine-fold in-plane undersampling in this example. In other words,
 90 the undersampling factor per segment linearly scales up with the number
 91 of shots. Consequently, conventional self-gating reconstruction techniques,
 92 e.g. MUSE, suffer from degraded shot-to-shot phase estimation, which in

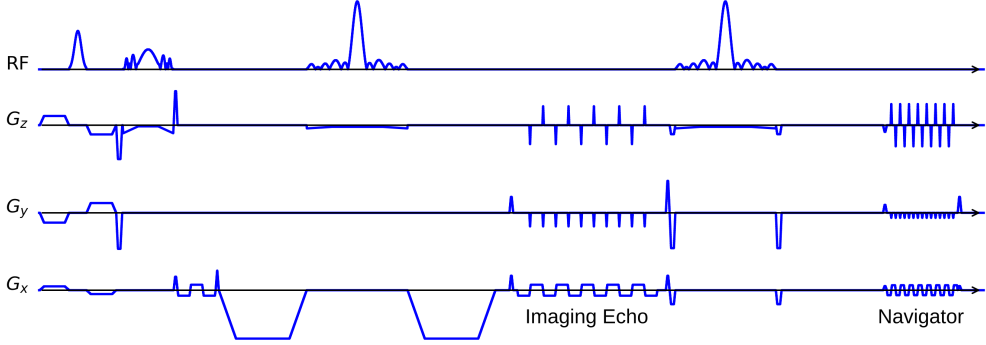


Figure 2: The NAViEPI sequence diagram. SMS is utilized for the acquisition of both imaging and navigator echoes. While the acceleration factor per navigator is the same as listed in Table 1, the acceleration factor per imaging echo is in addition linearly scaled by the number of shots.

93 turn limits the number of shots and spatial resolution.

94 *2.2. NAViEPI: Navigator-based iEPI with consistent effective ESP between
95 the imaging and the navigator echo - where iEPI meets rsEPI*

96 Instead of the self-gated MUSE with in-plane fully-sampled iEPI and
97 a limited number of shots, We propose NAVigator-based interleaved EPI
98 (NAViEPI), as illustrated in Fig. 2. Inspired by rsEPI (Porter and Hei-
99 demann, 2009), NAViEPI enforces a consistent effective ESP between the
100 imaging and the navigator echo, thereby minimizing distortion mismatch
101 between the two echoes.

102 Since one imaging echo presents one segment in multi-shot EPI acquisi-
103 tion, its effective ESP is defined as

$$\text{ESP}_{\text{eff}} = \frac{\text{ESP}}{R_{\text{in-plane}} \times N_{\text{shot}}} \quad (1)$$

104 Here, a larger number of shots (segments) increases the undersampling factor
105 per segment (see Fig. 1), but decreases the effective ESP. Since the navigator

106 echo is acquired for each segment, its in-plane undersampling factor equals
107 $R_{\text{in-plane}}$. Therefore, the effective ESP of the navigator echo must match that
108 of the imaging echo, as given in Eq. (1). With a matching effective ESP, the
109 base resolution of the navigator echo can then be determined.

110 *2.3. In vivo acquisition protocols*

111 We implemented multiple in-vivo acquisition protocols at a clinical 7 T
112 MR system (MAGNETOM Terra, Siemens Healthineers, Erlangen, Ger-
113 many) equipped with a 32-channel head coil (Nova Medical, Wilmington,
114 MA, USA) and the XR-gradient system (maximum gradient strength 80 mT/m
115 with a peak slew rate of 200 T/m/s). To calibrate coil sensitivity maps, refer-
116 ence scans employed a gradient-echo (GRE) sequence. Spectral fat saturation
117 and mono-polar diffusion-encoding gradients were used. The phase-encoding
118 direction was selected as anterior-to-posterior.

Table 1: NAViEPI acquisition protocols

Protocol	1.0 mm isotropic		sub-millimeter	
	#1	#2	#3	#4
Diffusion mode	MDDW ⁽¹⁾		3-scan trace	
Diffusion scheme	monopolar			
Diffusion direction	20	114	3	
<i>b</i> -value (s/mm ²)	1000	3-shell ⁽²⁾	1000	
<i>b</i> ₀	0	12	1	
FOV (mm ²)	200	214	220	
In-plane resolution (mm ²)	1.0		0.5	
Slice thickness (mm)	1.0		2.0	
Slices	141	114	60	
Navigator	No	No	Yes	No
Shots	4	2	5	1
TR (ms)	7700	5200	4400	8000
TEs (ms)	67	66	58/95.1	143
ESP (ms)	1.02	0.81	1.52	1.48
Bandwidth (Hz/Pixel)	1086	1460	758	
Partial Fourier			6/8	
Acceleration ⁽³⁾	1 × 3	3 × 3	3 × 2	
TA (min) ⁽⁴⁾	10 : 42	22 : 25	1 : 38	0 : 46

⁽¹⁾ MDDW: Multi-direction diffusion weighting;

⁽²⁾ 3-shell: 20, 30, and 64 directions with *b*-values of 1000, 2000, and 3000 s/mm², respectively;

⁽³⁾ Acceleration: Both in-plane and slice undersampling can be employed, denoted as (*R*_{in-plane} × *R*_{slice});

⁽⁴⁾ TA: Total acquisition time.

120 This study was approved by the local ethics committee. Three volunteers
121 with informed consent obtained before scanning participated in this
122 study. Detailed acquisition protocols are listed in Table 1. In the spirit of re-
123 producible research, another volunteer with informed consent was recruited
124 for the scan of all acquisition protocols, and the results were displayed in
125 Supplementary Information.

126 *2.3.1. 20-diffusion-direction acquisition at 1 mm isotropic resolution*

127 As listed in Table 1, Protocol #1 with four-shot iEPI and without in-
128 plane undersampling was implemented. This protocol represents the acquisi-
129 tion scheme employed in many existing multi-shot reconstruction techniques,
130 (e.g., MUSE, SPA-LLR, and JULEP). The acquired data from this protocol
131 served as ground truth. Different reconstruction methods, specifically JETS,
132 MUSE, and JULEP were compared. We compared with JULEP instead of
133 MUSSELS, because JULEP uses not only structured low-rank constraints
134 but also explicit phase mapping.

135 We then retrospectively reduced the four-shot data to only one shot per
136 diffusion encoding without and with the proposed k_y shifting to simulate
137 four-fold in-plane undersampling. JETS reconstruction was performed on
138 the fully-sampled data and the retrospectively undersampled data to validate
139 the proposed k_y -shifted acquisition.

140 *2.3.2. Three-shell acquisition at 1 mm isotropic resolution*

141 Protocol #2 in Table 1 was implemented for multi-shell diffusion tensor
142 imaging (DTI) (Basser et al., 1994). We acquired a total of 114 diffusion
143 directions, whereas b_0 measurements were interspersed every ten diffusion

₁₄₄ directions. This protocol was used to demonstrate the capability of JETS
₁₄₅ in achieving high spatial-angular-temporal resolution.

₁₄₆ *2.3.3. 3-scan trace acquisition at $0.5 \times 0.5 \times 2.0 \text{ mm}^3$ voxel size*

₁₄₇ As listed in Table 1, Protocol #3 was implemented based on NAViEPI
₁₄₈ with five shots per diffusion encoding. This protocol was compared against
₁₄₉ single-shot EPI (Protocol #4) with the same spatial resolution and acceler-
₁₅₀ ation, such as to demonstrate the sampling efficiency of NAViEPI.

₁₅₁ *2.4. Forward modeling*

₁₅₂ Our proposed acquisition method yields multi-dimensional multi-band
₁₅₃ k -space data $\mathbf{y}_{c,q,s}$, where c, q, s denotes the index of the coil sensitivity
₁₅₄ map, the diffusion encoding, and the shot, respectively. Acquisition modeling
₁₅₅ needs to consider several aspects.

₁₅₆ First, the acquired k -space data \mathbf{y} is mapped from individual shot images
₁₅₇ $\mathbf{x}_{q,s,z}$ via the forward model,

$$\begin{aligned} \mathbf{y}_{c,q,s} &= \mathbf{P}_{q,s} \boldsymbol{\Sigma} \boldsymbol{\Theta}_z \mathbf{F} \mathbf{S}_c \mathbf{x}_{q,s,z} \\ \mathbf{y} &:= \mathbf{E}_1 \mathbf{x} \end{aligned} \quad (2)$$

₁₅₈ Here, the encoding matrix \mathbf{E}_1 comprises a chain of linear operators. Every
₁₅₉ shot image \mathbf{x} is point-wise multiplied by a set of coil sensitivity maps (\mathbf{S}) and
₁₆₀ Fourier transformed (\mathbf{F}). The output is then point-wise multiplied by the
₁₆₁ multi-slice phase map ($\boldsymbol{\Theta}$) with z the slice index in simultaneously excited
₁₆₂ slices. This operator shifts individual slice along the phase-encoding direction
₁₆₃ via varying phase modulation (Breuer et al., 2005). The SMS k -space data

164 is then summed (collapsed, Σ) along the slice dimension and masked (point-
165 wise multiplied, \mathbf{P}) by the sampling pattern of each diffusion encoding and
166 shot.

167 Second, for diffusion MRI based on multi-shot EPI, multiple shots ac-
168 quired for a given diffusion encoding need to be combined as one DW image
169 ($\tilde{\mathbf{x}}$). One possibility is to perform magnitude average (Chen et al., 2013)
170 or root-sum-squares (RSS) (Mani et al., 2017) of shot images. This method
171 is robust to in-plane motion, but sub-optimal concerning SNR (Guhaniyogi
172 et al., 2016). Alternatively, shot combination can be done via shot-to-shot
173 phase variation correction (Liu et al., 2005; Chen et al., 2013). This can be
174 incorporated into our formulation as point-wise multiplication between the
175 shot-to-shot phase variation (Φ) and the DW image ($\tilde{\mathbf{x}}$),

$$\mathbf{x}_{q,s,z} = \Phi_{q,s,z} \tilde{\mathbf{x}}_{q,z} \quad (3)$$

176 Note that $\tilde{\mathbf{x}}$ can be obtained by applying the adjoint of Φ to \mathbf{x} . In MUSE,
177 Φ is obtained by parallel imaging reconstruction of all shots with subsequent
178 phase smoothing of every shot image. Based on this phase correction, the
179 complete forward model follows

$$\mathbf{y} := \mathbf{E}_2 \tilde{\mathbf{x}} = \mathbf{E}_1 \Phi \tilde{\mathbf{x}} \quad (4)$$

180 where the encoding matrix \mathbf{E}_2 comprises the chain of the shot-to-shot phase
181 variation Φ and the encoding matrix \mathbf{E}_1 . We implemented these two encoding
182 operators in SigPy (Ong and Lustig, 2019).

183 2.5. Joint k - q -slice reconstruction

184 Based on the generalized forward models in Eqs. (2) and (4), our proposed
185 joint k - q -slice reconstruction can be formulated as a three-step approach.

186 **I. Navigator echo reconstruction.** The acquisition of navigator echoes
 187 follows the forward model in Eq. (2), so the reconstruction of navigator
 188 echoes can be formulated as:

$$\operatorname{argmin}_{\mathbf{x}} \|\mathbf{y} - \mathbf{E}_1 \mathbf{x}\|_2^2 + \lambda \mathbf{R}(\mathbf{x}) \quad (5)$$

189 where $\mathbf{R}(\mathbf{x})$ denotes the regularization functional with the regularization
 190 strength λ . In this work, ℓ^2 regularization was used, i.e., $\mathbf{R}(\mathbf{x}) =$
 191 $\|\mathbf{x}\|_2^2$. In the case of self-navigating (i.e., no navigator acquired) as Pro-
 192 tocol #2, the central k -space region (i.e., 1/4 of the full image matrix)
 193 of each segment is used as \mathbf{y} in Eq. (5).

194 **II. Phase smoothing.** Shot-to-shot phase variation was extracted from
 195 the reconstructed navigator echo phases. Assuming that phase images
 196 are spatially smooth (Chen et al., 2013; Dai et al., 2023), we employed
 197 the adaptive Hanning filter to smooth shot phases,

$$\mathbf{x} = \mathbf{F}^{-1} \mathcal{H}^K \mathbf{F} \mathbf{x} \quad (6)$$

198 where x is the reconstructed navigator image from Step I. \mathcal{H} is the
 199 Hanning window with the non-negative integer K . K controls the width
 200 of the Hanning window.

201 **III. Shot-combined reconstruction.** Joint reconstruction of all DW im-
 202 ages using the shot-combined forward model \mathbf{E}_2 with shot-to-shot phase
 203 variation from Step II reads:

$$\operatorname{argmin}_{\tilde{\mathbf{x}}} \|\mathbf{y} - \mathbf{E}_2 \tilde{\mathbf{x}}\|_2^2 + \lambda \|\mathbf{T}(\tilde{\mathbf{x}})\|_* \quad (7)$$

204 Here, LLR regularization was employed in the local spatial-diffusion
 205 matrices, based on the theory of partially separable functions (Liang,

206 2007; Trzasko and Manduca, 2011; Zhang et al., 2015). \mathbf{T} represents
207 a linear operator that firstly slides a local patch window through all
208 DW images and then flattens every set of local patches to construct
209 two-dimensional (2D) spatial-diffusion matrices. The spatial dimension
210 equals the block size, and the diffusion dimension is the number of dif-
211 fusion encodings. $\|\mathbf{T}(\tilde{\mathbf{x}})\|_*$ is the nuclear norm, i.e. the sum of singular
212 values of a spatial-diffusion matrix. This nuclear norm regularization
213 was accomplished via singular value thresholding (SVT) of each spatial-
214 diffusion matrix (Cai et al., 2010). After SVT, the adjoint of \mathbf{T} , \mathbf{T}^H ,
215 was needed to reorder pixel values from the spatial-diffusion matrices
216 back to DW images.

217 To alleviate checkerboard artifacts induced by LLR regularization with
218 non-overlapping blocks (Hu et al., 2020), we employed overlapping blocks.
219 In this case, values from overlapping positions are summed up to the
220 output of \mathbf{T}^H . To enable the correct use of \mathbf{T}^H , we element-wise divided
221 the output of \mathbf{T}^H by a scaling matrix. This matrix was obtained via
222 $\mathbf{T}^H(\mathbf{T}(\mathbf{1}))$, where $\mathbf{1}$ denotes the matrix of all ones with the same shape
223 as the input \mathbf{x} .

224 As the local patch window varies depending on the number of diffusion
225 encodings or user selection, we implemented a singular-value spectrum
226 normalization strategy to reduce the effect of the local patch window
227 variation on regularization strength. Specifically, the singular values of
228 constructed spatial-diffusion matrices were divided by the patch window
229 width. After SVT, the thresholded singular values were multiplied with
230 the patch window width for rescaling.

231 2.6. Reconstruction

232 The acquired raw data was read in by twixtools (<https://github.com/pehses/twixtools>). Ramp-sampling regridding and FOV/2-ghost correction were also performed in twixtools. Subsequently, coil sensitivity maps were computed from reference scans using ESPIRiT (Uecker et al., 2014) in SigPy (Ong and Lustig, 2019).

237 With this pre-processing as well as the implemented forward models and proximal operator, the inverse problem in Eq. (7) was solved by the alternating direction method of multipliers (ADMM) (Boyd et al., 2010).

240 ADMM solves the minimization problems in an alternating update scheme,

$$\begin{cases} \mathbf{x}^{(k+1)} := \underset{\mathbf{x}}{\operatorname{argmin}} \| \mathbf{y} - \mathbf{E}(\mathbf{x}) \|^2 + \rho/2 \| \mathbf{T}\mathbf{x} - \mathbf{z}^{(k)} + \mathbf{u}^{(k)} \|_2^2 \\ \mathbf{z}^{(k+1)} := \mathcal{T}_{\lambda/\rho}(\mathbf{T}\mathbf{x}^{(k+1)} + \mathbf{u}^{(k)}) \\ \mathbf{u}^{(k+1)} := \mathbf{u}^{(k)} + \mathbf{T}\mathbf{x}^{(k+1)} - \mathbf{z}^{(k+1)} \end{cases} \quad (8)$$

241 where k denotes the ADMM iteration. \mathbf{z} is the auxiliary variable ($\mathbf{z} = \mathbf{T}\mathbf{x}$), and \mathbf{u} is the Lagrangian multipliers. Importantly, when solving Eq. (2), \mathbf{x} denotes shot images and \mathbf{E} denotes \mathbf{E}_1 in Eq. (8). In contrast, \mathbf{x} denotes shot-combined images and \mathbf{E} denotes \mathbf{E}_2 when solving Eq. (4). \mathbf{x} can be solved using linear least square algorithms, e.g. conjugate gradients (Hestenes and Stiefel, 1952), while \mathbf{z} is updated via singular value thresholding (\mathcal{T}) with the thresholding parameter λ/ρ . The coupling parameter ρ is effective in both the update of \mathbf{x} and \mathbf{z} . It acts as Tikhonov regularization strength when updating \mathbf{x} , but also inversely scales the thresholding strength when updating \mathbf{z} .

251 In this work, 15 ADMM iterations with $\rho = 0.05$ and $\lambda = 0.01$ were used.

252 All reconstructions were done on a single A100 SXM4/NVLink GPU with
253 40 GB memory (NVIDIA, Santa Clara, CA, USA).

254 We compared our proposed joint reconstruction with established multi-
255 shot reconstruction techniques, specifically, MUSE (Chen et al., 2013) and
256 JULEP (Dai et al., 2023), hosted on GitHub by Dr. Dai (Dai et al., 2023).
257 Further, we performed the local-PCA denoising (Cordero-Grande et al., 2019)
258 as implemented in MRtrix (Tournier et al., 2019) on the MUSE reconstructed
259 complex DW images.

260 The in vivo data acquired from Protocol #2 in Table 1 consisted of 126
261 diffusion directions, which exceeds the available GPU memory. Therefore,
262 the 126 data volumes were uniformly split into three parts for our JETS
263 reconstruction with a LLR block width of 6 and the LLR regularization in
264 both Steps I and III in Section 2.5. In addition, MUSE reconstruction was
265 also performed, followed by the local-PCA denoising. Reconstructed DWIs
266 were then processed by DiPy (Garyfallidis et al., 2014) to obtain color-coded
267 fractional anisotropy (cFA) maps.

268 **3. Results**

269 *3.1. Smoothing of shot-to-shot phase variation*

270 Navigators were acquired with the acceleration rate as listed in Table 1.
271 Besides, the base resolution of navigators (e.g. 32 in Protocol #3 in Table 1)
272 was smaller than imaging echoes. As a result, reconstructed navigator phases
273 (refer to the first column in Fig. 3) from Step I in Section 2.5 are not spatially
274 smooth. Such phases, when used in the shot-combined reconstruction, result
275 in signal void artifacts in DW images. To address this problem, we utilized
276 the phase smoothing procedure. As shown in Fig. 3, the ripple-like phase
277 artifact disappears at $K = 5$, while retaining the shot-to-shot phase variation.
278 In contrast, a larger K (e.g., $K = 20$) makes the filter too strong and partially
279 removes phase variation.

280 *3.2. Comparison to MUSE and JULEP with four-shot iEPI acquisition*

281 The iterative phase smoothing was also applicable to MUSE-type self-
282 navigating reconstruction, where shot phases were reconstructed from imag-
283 ing echoes. Fig. 4 compares our proposed JETS with MUSE (Chen et al.,
284 2013), MUSE with complex-valued local-PCA denoiser (Cordero-Grande et al.,
285 2019), and JULEP (Dai et al., 2023). The residual noise from MUSE can be
286 largely removed by the denoiser. However, when compared to JETS, the de-
287 noiser shows residual noise patterns within the globus pallidus (indicated by
288 the red arrow). JETS also shows better denoising than JULEP. The reason
289 is that JETS enforces spatial-diffusion regularization, whereas JULEP for-
290 mulates structured low-rank regularization of the four shots for one diffusion
291 encoding.

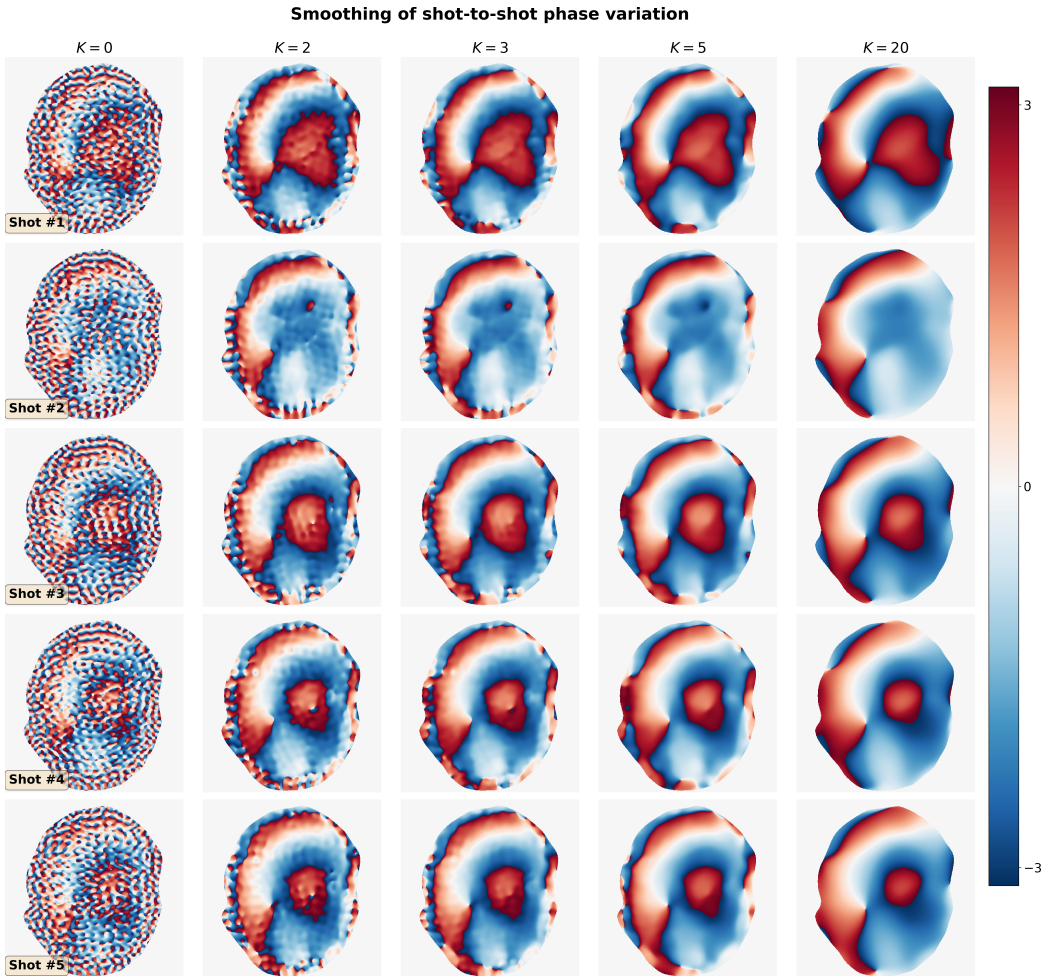


Figure 3: Smoothing of shot-to-shot phase variation according to Eq. (6). Navigators from Protocol #3 were reconstructed based on Step I in Section 2.5 and then used as the input (the column with $K = 0$).

8th DW image from 4-shot iEPI @ 1 mm ISO

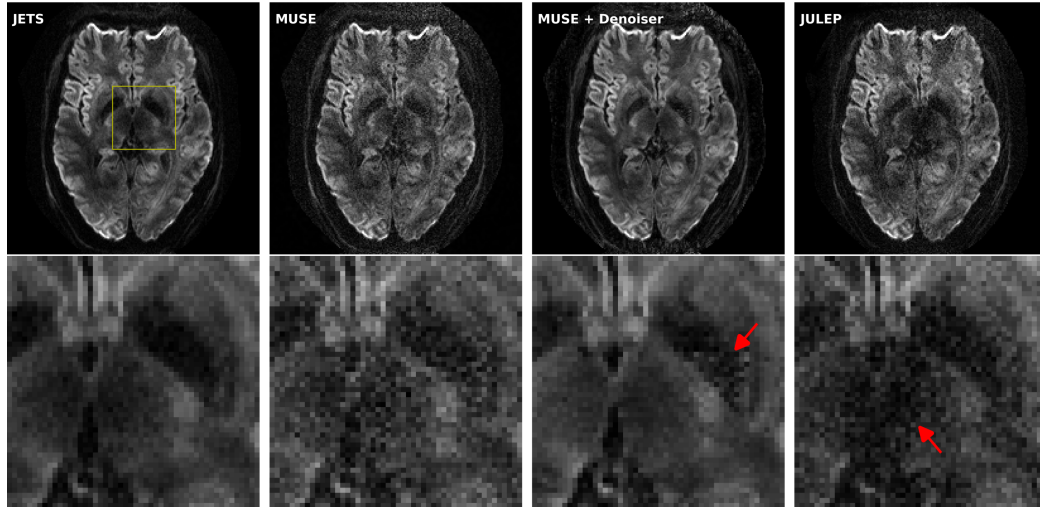


Figure 4: Reconstructed DW images (the 8th diffusion encoding) based on 4-shot iEPI acquisition with 1 mm isotropic resolution (Protocol #1 in Table 1). Four reconstruction methods are compared (from left to right): JETS, MUSE, MUSE with denoiser, and JULEP. The 2nd row displays the magnified views of the yellow square. The image from the denoiser (3rd column) shows residual noise patterns within the globus pallidus (indicated by the red arrow). The JULEP reconstruction (4th column) shows signal dropout in the central region (indicated by the red arrow).

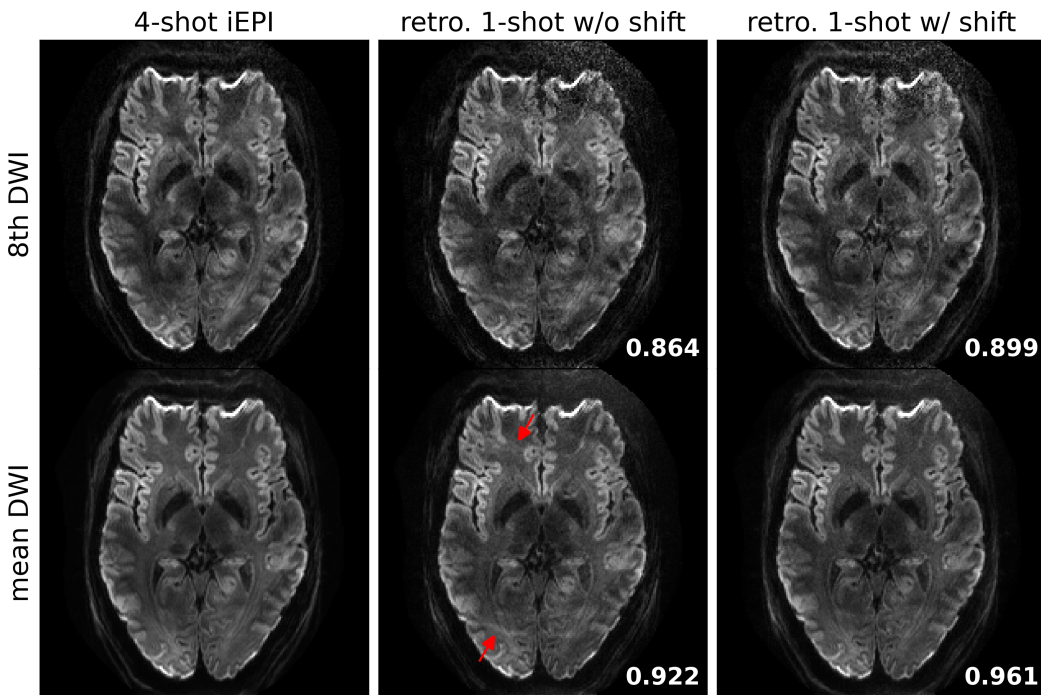


Figure 5: Quantitative validation of the proposed k_y -shift encoding sampling pattern based on 4-shot iEPI acquisition with 1 mm isotropic resolution (Protocol #1 in Table 1). (Top) the 8th diffusion encoding and (bottom) mean DWI over 20 diffusion encodings. (1st column) JETS reconstruction of 4-shot iEPI acquisition is used as the ground truth. The 2nd and the 3rd column displays JETS reconstruction of retrospectively undersampled 1-shot acquisition without and with k_y shifting, respectively. Residual aliasing artifacts are visible in the reconstruction without k_y shifting, as indicated by the red arrows. Structural similarity (SSIM) values are computed and displayed in the bottom right corners.

292 3.3. Retrospectively undersampling from the four-shot iEPI acquisition

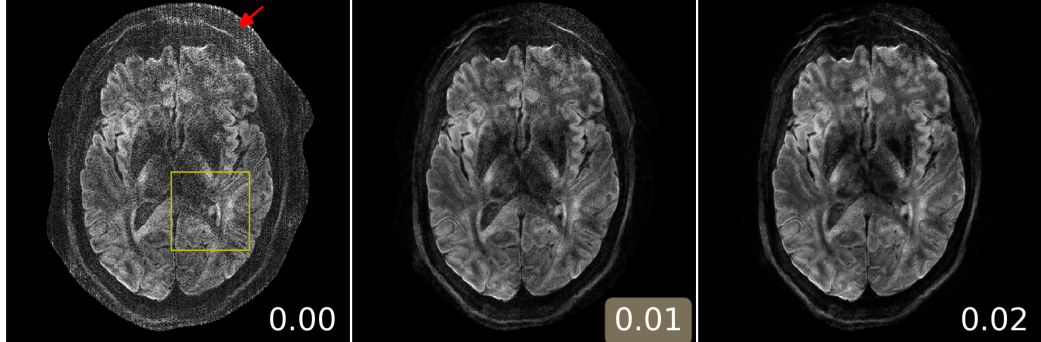
293 JETS reconstruction results on the four-shot prospectively fully-sampled
294 data from Protocol #1 in Table 1, as well as on the retrospectively under-
295 sampled one-shot data without and with the proposed k_y shift are displayed
296 in Fig. 5. Residual aliasing artifacts are visible in the reconstruction with-
297 out k_y shifting, as indicated by the red arrows. In contrast, the k_y shifting
298 scheme supplies a complementary k - q -space sampling pattern, which is bene-
299 ficial for joint reconstructions such as JETS. As shown in Fig. 5, JETS results
300 in improved SSIM values and reduced aliasing artifacts, when compared to
301 the reconstruction without k_y shifting. Figs. 4 and 5 show a slice containing
302 the globus pallidus with strong T_2 -weighted contrast and highlighting the
303 advantage of k_y -shift encoding in reducing undersampling artifacts.

304 3.4. Analysis of reconstruction parameters

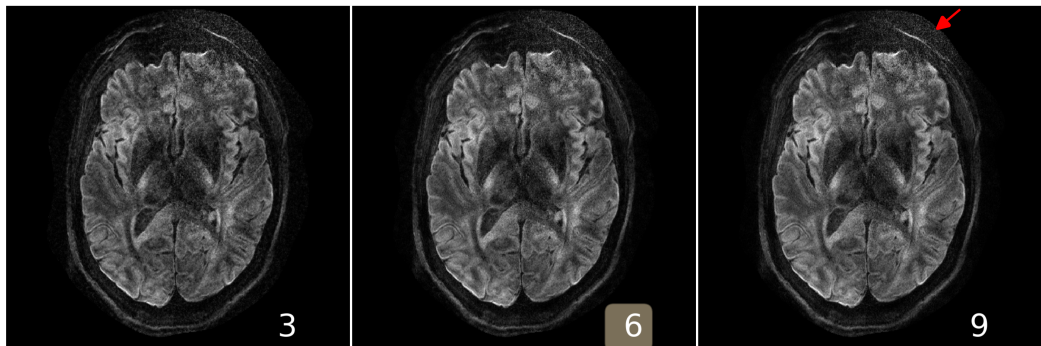
305 Here we provide a systematic analysis of the proposed JETS reconstruc-
306 tion with LLR regularization applied to the spatial-diffusion dimension, as
307 shown in Fig. 6.

308 First, we varied the regularization strength λ . We tested values of 0, 0.01,
309 and 0.02. The reconstruction with $\lambda = 0$ in Eq. (7) corresponds to parallel R1116.9a)
310 imaging reconstruction without LLR regularization. It is worth noting that
311 the proposed NAViEPI sequence demonstrates high-quality sub-millimeter
312 DW images ($0.5 \times 0.5 \times 2.0 \text{ mm}^3$ in this example). The DW images can be
313 further improved with the use of LLR regularization, i.e., reduced noise, as
314 seen in the reconstruction with $\lambda = 0.01$. Increasing λ (e.g. 0.02) further
315 reduces noise, but at the cost of increased blurring. Therefore, $\lambda = 0.01$ was
316 selected in this work.

(A) varying λ , keeping block as 6 and stride as 1



(B) varying block width, keeping λ 0.01 and stride as 1



(C) varying stride, keeping λ as 0.01 and block as 6

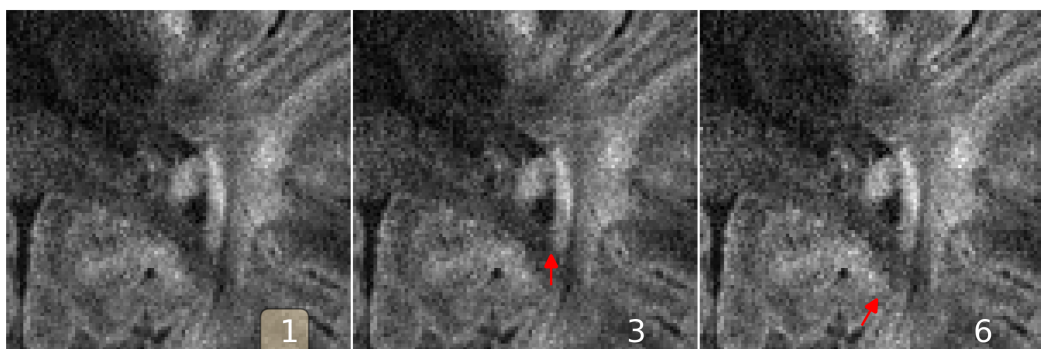


Figure 6: Analysis of reconstruction parameters based on the 3-scan trace acquisition with $0.5 \times 0.5 \times 2.0 \text{ mm}^3$ (Protocol #3 in Table 1). Displayed are JETS reconstructed single-direction DW images. **(A)** Varying the regularization strength λ from 0 to 0.01 and 0.02. **(B)** Varying the block width from 3 to 6 and 9. The red arrow indicates increased noise with the large block width. **(C)** Varying the stride size from 1 to 3 (partially overlapping) and 6 (non-overlapping). The red arrows indicate blocky artifacts.

317 Second, besides the regularization strength, we varied the block width.
318 Reconstruction results for the data from Protocols #3 and #2 in Table 1 are R1116.9b)

319 displayed in Fig. 6 (B) and Supporting Information Figure S6, respectively.
320 With the above-mentioned normalization strategy, the reconstruction results
321 show similar denoising effects. However, small block width (i.e., 3) suffers
322 from residual blurring artifacts, as shown in SI Figure S6. Therefore, the
323 block width of 6 was selected in this work.

324 Third, we varied the stride, i.e., the step from one local patch to the
325 next. The use of overlapping LLR (Fig. 6 (C) left) better suppresses blocky
326 artifacts, compared to the partially overlapping (stride < block) LLR (Fig. 6
327 (C) middle) and the non-overlapping (stride = block) LLR (Fig. 6 (C) right).

328 *3.5. Sampling efficiency of NAViEPI*

329 As shown in Fig. 7, NAViEPI achieves sub-millimeter resolution (voxel
330 size $0.5 \times 0.5 \times 2.0 \text{ mm}^3$) with the use of a 5-shot acquisition. When compared
331 to a single-shot acquisition with the same voxel size, the acquisition time of
332 NAViEPI is about two times longer, but the image quality of NAViEPI is
333 remarkably improved.

334 In the sub-millimeter imaging scenario, the increased base resolution re-
335 quires longer TE (143 ms) in the single-shot acquisition, which results in
336 significant signal loss due to T_2 relaxation. Therefore, sub-millimeter DWI
337 necessitates multi-shot acquisition, which is subject to shot-to-shot phase
338 variation and long scan time. However, NAViEPI solves both challenges. The
339 5-shot acquisition reduces TE to 58 ms, and thus retains SNR significantly
340 compared to the single-shot acquisition. Moreover, the JETS reconstruction
341 can help to reduce noise and improve structural visibility.

3-scan trace acquisition with voxel size $0.5 \times 0.5 \times 2.0 \text{ mm}^3$

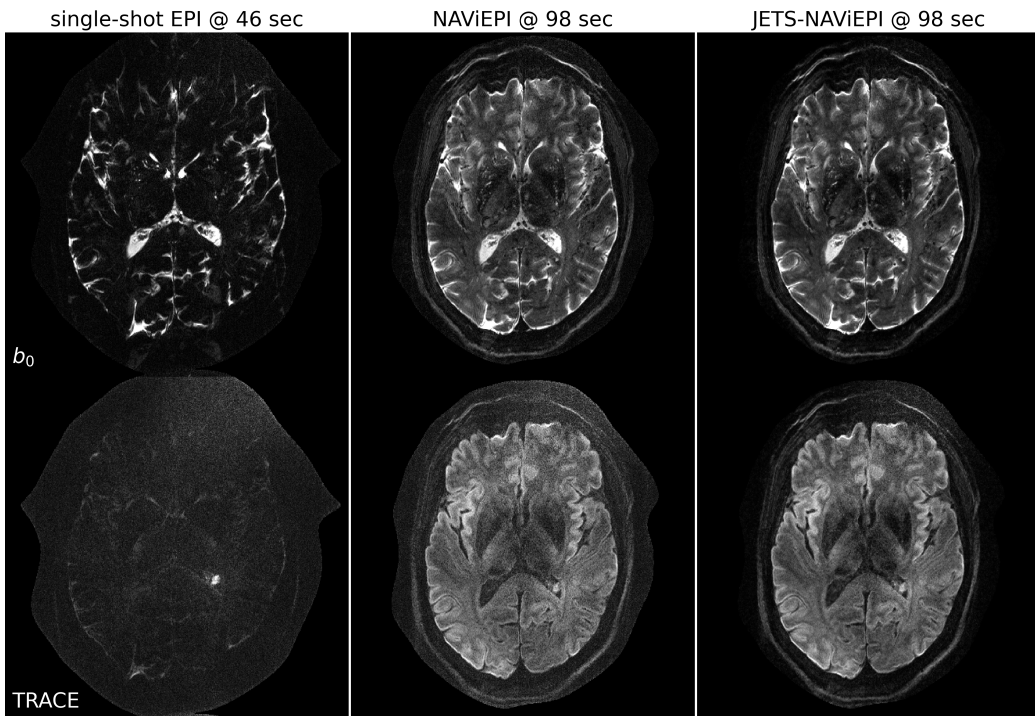


Figure 7: Sampling efficiency of the proposed NAViEPI sequence. 5-shot NAViEPI acquisition with the voxel size $0.5 \times 0.5 \times 2.0 \text{ mm}^3$ (Protocol #3) was compared with single-shot EPI acquisition (Protocol #4). Both the 1st and the 2nd columns were reconstructed via parallel imaging without LLR regularization, whereas the 3rd column was reconstructed via JETS.

3-scan trace acquisition with voxel size $0.5 \times 0.5 \times 2.0 \text{ mm}^3$

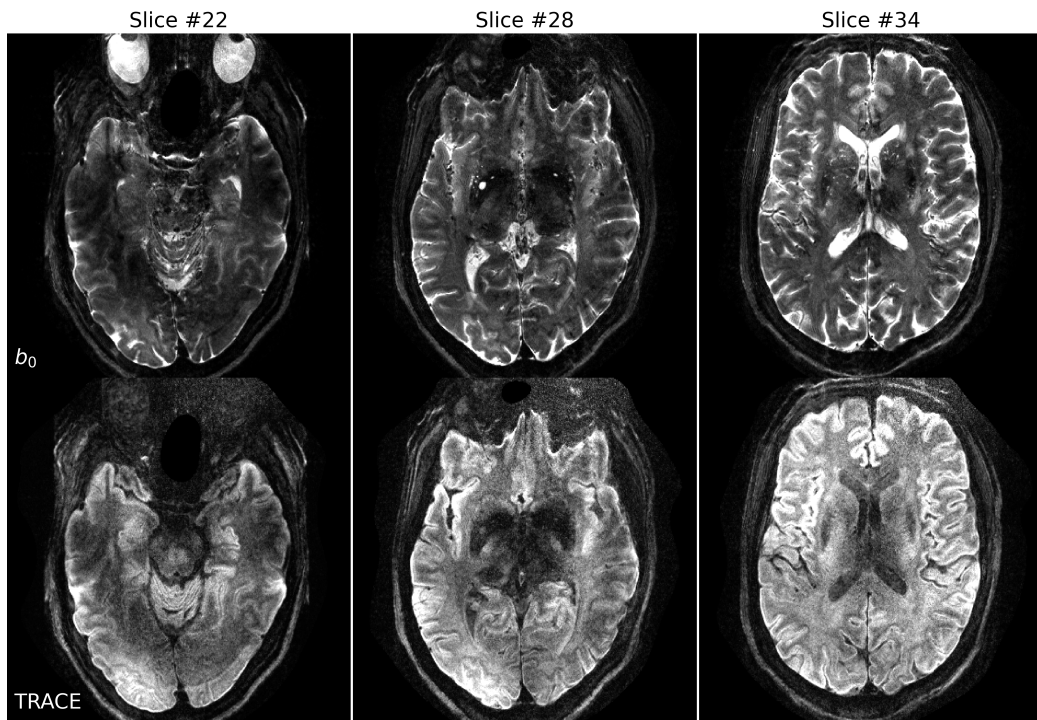


Figure 8: Reconstruction of the 3-scan trace acquisition with the voxel size $0.5 \times 0.5 \times 2.0 \text{ mm}^3$ (Protocol #3) at different slices.

342 Fig. 8 shows the JETS reconstructed b_0 and TRACE images in different
343 slice locations. Admittedly, the lower brain region (e.g. slice #22) exhibits in-
344 homogeneous and lower signal intensity than the upper slices. Such inhomog-
345 eneity can be alleviated with the use of multi-channel parallel transmission
346 (Katscher et al., 2003; Grissom et al., 2010).

347 Here, Figs. 6 and 7 show a slice with a benign lesion (the circular bright
348 spot) within the left ventricle. Fig. 8 displays three representative slices:
349 (left) an inferior brain region with marked B_1^+ field inhomogeneity, (mid-
350 dle) the middle brain slice which shows susceptibility artifacts in the frontal
351 region, and (right) a superior brain slice which shows the ventricle.

352 *3.6. Diffusion tensor imaging*

353 Protocol #2 in Table 1 yields an acceleration factor of 6×3 per shot, re-
354 sulting in severe noise amplification in MUSE reconstructed DWIs, as shown
355 in Fig. 9. Here, a slice that highlights the corpus callosum is displayed, and
356 the diffusion direction at the b -value of 3000 s/mm^2 with bright signal within
357 the corpus callosum is shown. The local-PCA denoiser substantially removes
358 noise, but the DWI at high b -values still illustrates more noise, compared to
359 the proposed JETS reconstruction. On the other hand, we applied the local-
360 PCA denoiser before the shot combination in MUSE. As shown in Fig. 9,
361 this approach is less effective compared to the application of the denoiser
362 after the shot combination, because shot images were reconstructed from the
363 central k -space region and have a coarse resolution.

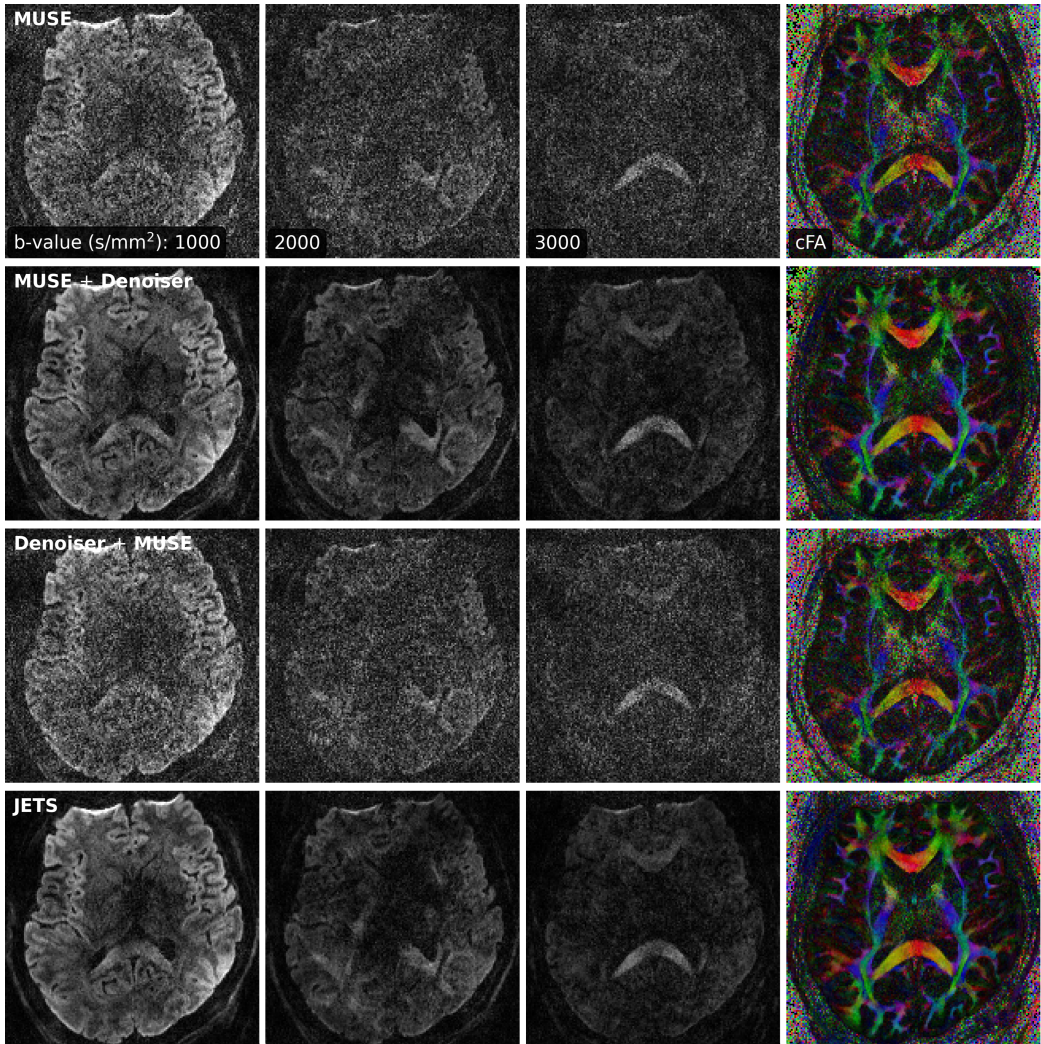


Figure 9: Comparison of three-shell DWIs and cFA maps with data acquired by Protocol #2 in Table 1. Reconstruction methods from top to bottom were MUSE, MUSE with the local-PCA denoiser, the application of the denoiser on shot images before the shot combination in MUSE, and the proposed JETS method.

364 **4. Discussion**

365 This work reports a novel DW-MRI technique, JETS-NAViEPI. NAViEPI
366 (1) achieves the fast and efficient acquisition of both imaging and navigator
367 echoes, (2) enforces consistent effective ESP between the two echoes, and (3)
368 allows for undersampled iEPI as well as a large number of shots. Moreover,
369 compared to the single-shot acquisition, joint k - q -slice reconstruction with k_y -
370 shift encoding on NAViEPI retains SNR and reduces aliasing artifacts in DW
371 images. As a result, JETS-NAViEPI renders high spatiotemporal resolution
372 diffusion MRI protocols in 7 T, e.g., a 3-scan trace acquisition with the voxel
373 size $0.5 \times 0.5 \times 2.0 \text{ mm}^3$ at 1.5 min.

374 One limitation of JETS-NAViEPI is the long reconstruction time due to
375 the simultaneous reconstruction of all DW images and the use of overlapping
376 locally low-rank regularization. The reconstruction for the Protocol #3 in
377 Table 1 on an A100 GPU takes about 2 min per multi-band slice. To reduce
378 the computation time, coil compression algorithms (Buehrer et al., 2007;
379 Huang et al., 2008) can be employed to reduce the number of coils for image
380 reconstruction. Moreover, one can deploy multi-GPU distributed computing
381 or modern optimization algorithms (e.g. stochastic gradient descent) (Ong
382 et al., 2020) to speed up the reconstruction.

383 Neither the signal modeling in Eqs. (2) and (4) nor the LLR regulariza-
384 tion considers the subject motion. In the presence of motion, the regularized
385 reconstruction can degrade. To overcome this problem, scout-informed mo-
386 tion estimation and reconstruction (Polak et al., 2022) could be integrated
387 into the framework.

388 Another potential extension of this work is to incorporate distortion cor-

389 rection. The standard distortion correction method is known as TOPUP
390 ([Andersson et al., 2003](#)), which acquires two scans with opposing phase-
391 encoding directions to obtain the field inhomogeneity map and then per-
392 forms conjugate phase reconstruction to correct for distortion. Alternatively,
393 a multi-echo acquisition could be used for the coil sensitivity reference scan,
394 such that both coil sensitivity and B_0 field inhomogeneity maps could be
395 reconstructed from the data.

396 This work employed a single regularization weight λ to enforce low rank-
397 ness along the spatial-diffusion direction. However, SNR may be heteroge-
398 neous within the FOV. Therefore, one single regularization scalar may be
399 inadequate to cover the whole FOV. Beyond this SVT-based reconstruction,
400 one can seek to use machine learning to learn a q -space prior as the regularizer
401 ([Hammernik et al., 2018; Lam et al., 2019; Mani et al., 2021](#)).

402 Although NAViEPI employs navigators for the acquisition of shot-to-
403 shot phase variation, it is worth noting that phase behavior depends on
404 several hard-to-control factors such as pulsatile motion, bulk motion, loca-
405 tions within the brain, and diffusion sensitization strength. Therefore, more
406 comprehensive modeling or post-processing such as image registration can
407 be considered in future work.

408 This work compared LLR regularized JETS to MUSE post-processed by
409 the local PCA denoiser ([Cordero-Grande et al., 2019](#)). Both the LLR reg-
410 ularization and the local PCA denoiser are based on the principle that low
411 rankness exists in the spatial-diffusion dimension ([Moeller et al., 2021](#)), where
412 the spatial content is extracted from local patches within the full image vol-
413 ume and the diffusion dimension is from the q -space encoding. One could

414 integrate the automatic noise estimation based on the Marchenko-Pastur law
415 for the determination of the thresholds in the LLR regularization to synergize
416 these two methods.

417 While this work reconstructs all DW images and then performs model
418 fitting, an alternative approach is to directly estimate b_0 and diffusion ten-
419 sors from measured k - q -space data using model-based reconstruction ([Knoll et al., 2015](#); [Dong et al., 2018](#); [Shafieizargar et al., 2023](#)). Compared to DW
420 image reconstruction, model-based reconstruction solves for a fewer number
421 of unknowns, but requires strict diffusion tensor modeling and the use of
422 nonlinear least square solvers.
423

424 **5. Conclusions**

425 We demonstrated the JETS-NAViEPI technique, which integrates a k_y -
426 shifted encoding navigator-based interleaved EPI sequence and joint recon-
427 struction with overlapping locally low-rank regularization for high spatial-
428 angular-temporal resolution DW-MRI at 7 T. This technique allows for high-
429 quality DW image reconstruction with accelerated acquisitions.

430 **Funding**

431 Funding by the German Research Foundation (DFG) is gratefully ac-
432 knowledged (projects 513220538, 512819079; and project 500888779 of the
433 RU5534 MR biosignatures at UHF). In addition, funding by the National
434 Institutes of Health (NIH), R01 EB024532 and P41 EB017183, is gratefully
435 acknowledged.

436 In addition, we gratefully acknowledge the scientific support and HPC
437 resources provided by the Erlangen National High Performance Computing
438 Center (NHR@FAU) of Friedrich-Alexander-University Erlangen-Nuremberg
439 (FAU) under the NHR project b143dc. NHR funding is provided by federal
440 and Bavarian state authorities. NHR@FAU hardware is partially funded by
441 the German Research Foundation (DFG) – 440719683.

442 **Data and code available statement**

443 In the spirit of reproducible and open science, we publish our source code
444 (<https://github.com/ZhengguoTan/sigpy>) as well as the raw k -space data
445 (<https://doi.org/10.5281/zenodo.10474402>). We also provide interac-
446 tive demonstrations of the reconstruction procedure (<https://github.com/>
447 [ZhengguoTan/NAViEPI](#)).

448 **Acknowledgments**

449 The authors thank Dr. Peter Neher for the discussion on MITK-Diffusion.
450 The authors thank Dr. Berkin Bilgic for making the MUSSELS source code
451 (<https://bit.ly/2QgBg9U>) publically available, Dr. Erpeng Dai for sharing
452 the JULEP source code (<https://github.com/daiep/JULEP>) on GitHub,
453 and Dr. Zhiyong Zhang for sharing the SPA-LLR source code (<https://github.com/ZZgroupSJTU/PMCmsDTI>) on GitHub. The authors also thank
454 Dr. Philipp Ehses for the discussion on twixtools ([https://github.com/](https://github.com/pehses/twixtools)
456 [pehses/twixtools](#)).

457 **References**

- 458 Andersson, J.L.R., Skare, S., Ashburner, J., 2003. How to correct suscepti-
459 bility distortions in spin-echo echo-planar images: application to diffusion
460 tensor imaging. *NeuroImage* 20, 870–888. doi:[10.1016/S1053-8119\(03\)00336-7](https://doi.org/10.1016/S1053-8119(03)00336-7).
- 462 Bammer, R., Keeling, S.L., Augustin, M., Pruessmann, K.P., Wolf, R., Stoll-
463 berger, R., Hartung, H.P., Fazekas, F., 2001. Improved diffusion-weighted
464 single-shot echo-planar imaging (EPI) in stroke using sensitivity encoding
465 (SENSE). *Magn. Reson. Med.* 46, 548–554. doi:[10.1002/mrm.1226](https://doi.org/10.1002/mrm.1226).
- 466 Basser, P.J., Mattiello, J., Le Bihan, D., 1994. MR diffusion tensor
467 spectroscopy and imaging. *Biophys. J.* 66, 259–267. doi:[10.1016/S0006-3495\(94\)80775-1](https://doi.org/10.1016/S0006-3495(94)80775-1).
- 469 Bilgic, B., Chatnuntawech, I., Manhard, M.K., Tian, Q., Liao, C., Iyer, S.S.,
470 Cauley, S.F., Huang, S.Y., Polimeni, J.R., Wald, L.L., Setsompop, K.,
471 2019. Highly accelerated multishot echo planar imaging through synergistic
472 machine learning and joint reconstruction. *Magn. Reson. Med.* 82, 1343–
473 1358. doi:[10.1002/mrm.27813](https://doi.org/10.1002/mrm.27813).
- 474 Block, K.T., Uecker, M., Frahm, J., 2007. Undersampled radial MRI with
475 multiple coils. Iterative image reconstruction using a total variation con-
476 straint. *Magn. Reson. Med.* 57, 1186–1098. doi:[10.1002/mrm.21236](https://doi.org/10.1002/mrm.21236).
- 477 Boyd, S., Parikh, N., Chu, E., Peleato, B., Eckstein, J., 2010. Distributed
478 optimization and statistical learning via the alternating direction method

- 479 of multipliers. Foundations and Trends in Machine Learning 3, 1–122.
480 doi:[10.1561/2200000016](https://doi.org/10.1561/2200000016).
- 481 Breuer, F.A., Blaimer, M., Heidemann, R.M., Mueller, M.F., Griswold, M.A.,
482 Jakob, P.M., 2005. Controlled aliasing in parallel imaging results in higher
483 acceleration (CAIPIRINHA) for multi-slice imaging. Magn. Reson. Med.
484 53, 684–691. doi:[10.1002/mrm.20401](https://doi.org/10.1002/mrm.20401).
- 485 Buehrer, M., Pruessmann, K.P., Boesiger, P., Kozerke, S., 2007. Array com-
486 pression for MRI with large coil arrays. Magn. Reson. Med 57, 1131–1139.
487 doi:[10.1002/mrm.21237](https://doi.org/10.1002/mrm.21237).
- 488 Butts, K., Riederer, S.J., Ehman, R.L., Thompson, R.M., Jack, C.R., 1993.
489 Interleaved echo planar imaging on a standard MRI system. Magn. Reson.
490 Med. 31, 67–72. doi:[10.1002/mrm.1910310111](https://doi.org/10.1002/mrm.1910310111).
- 491 Cai, J.F., Candès, E.J., Shen, Z., 2010. A singular value threshold-
492 ing algorithm for matrix completion. SIAM. J. Optim. 20, 1956–1982.
493 doi:[10.1137/080738970](https://doi.org/10.1137/080738970).
- 494 Chen, N.K., Guidon, A., Chang, H.C., Song, A.W., 2013. A robust multi-
495 shot scan strategy for high-resolution diffusion weighted MRI enabled by
496 multiplexed sensitivity-encoding (MUSE). NeuroImage 72, 41–47. doi:[10.1016/j.neuroimage.2013.01.038](https://doi.org/10.1016/j.neuroimage.2013.01.038).
- 498 Cordero-Grande, L., Christiaens, D., Hutter, J., Price, A.N., Hajnal, J.V.,
499 2019. Complex diffusion-weighted image estimation via matrix recovery
500 under general noise models. NeuroImage 200, 391–404. doi:[10.1016/j.neuroimage.2019.06.039](https://doi.org/10.1016/j.neuroimage.2019.06.039).

- 502 Dai, E., Ma, X., Zhang, Z., Yuan, C., Guo, H., 2017. Simultaneous multislice
503 accelerated interleaved EPI DWI using generalized blipped-CAIPI acqui-
504 sition and 3D K-space reconstruction. Magn. Reson. Med. 77, 1593–1605.
505 doi:[10.1002/mrm.26249](https://doi.org/10.1002/mrm.26249).
- 506 Dai, E., Mani, M., McNab, J.A., 2023. Multi-band multi-shot diffu-
507 sion MRI reconstruction with joint usage of structured low-rank con-
508 straints and explicit phase mapping. Magn. Reson. Med. 89, 95–111.
509 doi:[10.1002/mrm.29422](https://doi.org/10.1002/mrm.29422).
- 510 Dai, E., Zhang, Z., Ma, X., Dong, Z., Li, X., Xiong, Y., Yuan, C., Guo, H.,
511 2018. The effects of navigator distortion and noise level on interleaved EPI
512 DWI reconstruction: a comparison between image- and *k*-space method.
513 Magn. Reson. Med. 80, 2024–2032. doi:[10.1002/mrm.27190](https://doi.org/10.1002/mrm.27190).
- 514 Dong, Z., Dai, E., Wang, F., Zhang, Z., Ma, X., Yuan, C., Guo, H., 2018.
515 Model-based reconstruction for simultaneous multislice and parallel imag-
516 ing accelerated multishot diffusion tensor imaging. Med. Phys. 45, 3196–
517 3204. doi:[10.1002/mp.12974](https://doi.org/10.1002/mp.12974).
- 518 Garyfallidis, E., Brett, M., Amirbekian, B., Rokem, A., van der Walt, S.,
519 Descoteaux, M., Nimmo-Smith, I., Contributors, D., 2014. DIPY, a library
520 for the analysis of diffusion MRI data. Front. Neuroinform. 8, 1–17. doi:[10.3389/fninf.2014.00008](https://doi.org/10.3389/fninf.2014.00008).
- 522 Grissom, W.A., Sacolick, L., Vogel, M.W., 2010. Improving high-field MRI
523 using parallel excitation. Imaging Med. 2, 675–693. doi:[10.2217/IIM.10.62](https://doi.org/10.2217/IIM.10.62).

- 525 Griswold, M.A., Jakob, P.M., Heidemann, R.M., Nittka, M., Jellus, V.,
526 Wang, J., Kiefer, B., Haase, A., 2002. Generalized autocalibrating par-
527 tially parallel acquisitions (GRAPPA). Magn. Reson. Med. 47, 1202–1210.
528 doi:[10.1002/mrm.10171](https://doi.org/10.1002/mrm.10171).
- 529 Guhaniyogi, S., Chu, M.L., Chang, H.C., Song, A.W., Chen, N.K., 2016. Mo-
530 tion immune diffusion imaging using augmented MUSE for high-resolution
531 multi-shot EPI. Magn. Reson. Med. 75, 639–652. doi:[10.1002/mrm.25624](https://doi.org/10.1002/mrm.25624).
- 532 Hammernik, K., Klatzer, T., Kobler, E., Recht, M.P., Sodickson, D.K., Pock,
533 T., Knoll, F., 2018. Learning a variational network for reconstruction of
534 accelerated MRI data. Magn. Reson. Med. 79, 3055–3071. doi:[10.1002/mrm.26977](https://doi.org/10.1002/mrm.26977).
- 536 Heidemann, R.M., Porter, D.A., Anwander, A., Feiweier, T., Heberlein, K.,
537 Knösche, T.R., Turner, R., 2010. Diffusion imaging in humans at 7 T
538 using readout-segmented EPI and GRAPPA. Magn. Reson. Med. 64, 9–
539 14. doi:[10.1002/mrm.22480](https://doi.org/10.1002/mrm.22480).
- 540 Hestenes, M.R., Stiefel, E., 1952. Methods of conjugate gradients for solving
541 linear systems. J. Res. Natl. Bur. Stand. 49, 409–436. doi:[10.6028/jres.049.044](https://doi.org/10.6028/jres.049.044).
- 543 Hu, Y., Wang, X., Tian, Q., Yang, G., Daniel, B., McNab, J., Hargreaves, B.,
544 2020. Multi-shot diffusion-weighted MRI reconstruction with magnitude-
545 based spatial-angular locally low-rank regularization (SPA-LLR). Magn.
546 Reson. Med. 83, 1596–1607. doi:[10.1002/mrm.28025](https://doi.org/10.1002/mrm.28025).

- 547 Huang, F., Vijayakumar, S., Li, Y., Hertel, S., Duensing, G.R., 2008. A soft-
548 ware channel compression technique for faster reconstruction with many
549 channels. *Magn. Reson. Imaging* 26, 133–141. doi:[10.1016/j.mri.2007.04.010](https://doi.org/10.1016/j.mri.2007.04.010).
- 550
- 551 Jeong, H.K., Gore, J.C., Anderson, A.W., 2013. High-resolution human
552 diffusion tensor imaging using 2-D navigated multishot SENSE EPI at 7
553 T. *Magn. Reson. Med.* 69, 793–802. doi:[10.1002/mrm.24320](https://doi.org/10.1002/mrm.24320).
- 554 Jones, D.K., 2010. Diffusion MRI: Theory, methods, and applications. Oxford
555 University Press. doi:[10.1093/med/9780195369779.001.0001](https://doi.org/10.1093/med/9780195369779.001.0001).
- 556 Katscher, U., Börnert, P., Leussler, C., van den Brink, J.S., 2003. Transmit
557 SENSE. *Magn. Reson. Med.* 49, 144–150. doi:[10.1002/mrm.10353](https://doi.org/10.1002/mrm.10353).
- 558 Knoll, F., Raya, J.G., Halloran, R.O., Baete, S., Sigmund, E., Bammer, R.,
559 Block, T., Otazo, R., Sodickson, D.K., 2015. A model-based reconstruction
560 for undersampled radial spin-echo DTI with variational penalties on the
561 diffusion tensor. *NMR Biomed* 28, 353–366. doi:[10.1002/nbm.3258](https://doi.org/10.1002/nbm.3258).
- 562 Lam, F., Li, Y., Peng, X., 2019. Constrained magnetic resonance spectro-
563 scopic imaging by learning nonlinear low-dimensional models. *IEEE Trans.*
564 *Med. Imaging* 39, 545–555. doi:[10.1109/TMI.2019.2930586](https://doi.org/10.1109/TMI.2019.2930586).
- 565 Le Bihan, D., Breton, E., Lallemand, D., Grenier, P., Cabanis, E., Laval-
566 Jeantet, M., 1986. MR imaging of intravoxel incoherent motions: appli-
567 cation to diffusion and perfusion in neurologic disorders. *Radiology* 161,
568 401–407. doi:[10.1148/radiology.161.2.3763909](https://doi.org/10.1148/radiology.161.2.3763909).

- 569 Liang, Z.P., 2007. Spatiotemporal imaging with partially separable functions,
570 in: 2007 4th IEEE International Symposium on Biomedical Imaging: From
571 Nano to Macro, pp. 988–991. doi:[10.1109/ISBI.2007.357020](https://doi.org/10.1109/ISBI.2007.357020).
- 572 Liu, C., Moseley, M.E., Bammer, R., 2005. Simultaneous phase cor-
573 rection and SENSE reconstruction for navigated multi-shot DWI with
574 non-Cartesian k -space sampling. Magn. Reson. Med. 54, 1412–1422.
575 doi:[10.1002/mrm.20706](https://doi.org/10.1002/mrm.20706).
- 576 Lustig, M., Donoho, D., Pauly, J.M., 2007. Sparse MRI: The application of
577 compressed sensing for rapid MR imaging. Magn. Reson. Med. 58, 1182–
578 1195. doi:[10.1002/mrm.21391](https://doi.org/10.1002/mrm.21391).
- 579 Mani, M., Jacob, M., Kelley, D., Magnotta, V., 2017. Multi-shot sensitivity-
580 encoded diffusion data recovery using structured low-rank matrix comple-
581 tion (MUSSELS). Magn. Reson. Med. 78, 494–507. doi:[10.1002/mrm.26382](https://doi.org/10.1002/mrm.26382).
- 583 Mani, M., Magnotta, V.A., Jacob, M., 2021. qModeL: A plug-and-play
584 model-based reconstruction for highly accelerated multi-shot diffusion MRI
585 using learned priors. Magn. Reson. Med. 86, 835–851. doi:[10.1002/mrm.28756](https://doi.org/10.1002/mrm.28756).
- 587 Mansfield, P., 1977. Multi-planar image formation using NMR spin echoes.
588 J Phys C 10, 55–58. doi:[10.1088/0022-3719/10/3/004](https://doi.org/10.1088/0022-3719/10/3/004).
- 589 Maudsley, A.A., 1980. Multiple-line-scanning spin density imaging. J. Magn.
590 Reson. 41, 112–126. doi:[10.1016/0022-2364\(80\)90207-3](https://doi.org/10.1016/0022-2364(80)90207-3).

- 591 Merboldt, K.D., Hanicke, W., Frahm, J., 1985. Self-diffusion NMR imaging using stimulated echoes. *J. Magn. Reson.* 64, 479–486. doi:[10.1016/0022-2364\(85\)90111-8](https://doi.org/10.1016/0022-2364(85)90111-8).
- 594 Moeller, S., Pisharady, P.K., Ramanna, S., Lenglet, C., Wu, X., Dowdle, L., Yacoub, E., Uğurbil, K., Akçakaya, M., 2021. NOise reduction with DIistribution Corrected (NORDIC) PCA in dMRI with complex-valued 596 parameter-free locally low-rank processing. *NeuroImage* 226, 117539. 597 doi:[10.1016/j.neuroimage.2020.117539](https://doi.org/10.1016/j.neuroimage.2020.117539).
- 599 Mori, S., Crain, B.J., Chacko, V.P., Van Zijl, P.C.M., 1999. Three- 600 dimensional tracking of axonal projections in the brain by mag- 601 netic resonance imaging. *Ann. Neurol.* 45, 265–269. doi:[10.1002/1531-8249\(199902\)45:2<265::AID-ANA21>3.0.CO;2-3](https://doi.org/10.1002/1531-8249(199902)45:2<265::AID-ANA21>3.0.CO;2-3).
- 603 Ong, F., Lustig, M., 2019. SigPy: A Python package for high performance 604 iterative reconstruction, in: Proceedings of the 27th Annual Meeting of 605 ISMRM, Montréal, CAN, p. 4819. doi:[10.5281/zenodo.5893788](https://doi.org/10.5281/zenodo.5893788).
- 606 Ong, F., Zhu, X., Cheng, J.Y., Johnson, K.M., Larson, P.E.Z., Vasanawala, 607 S.S., Lustig, M., 2020. Extreme MRI: Large-scale volumetric dynamic 608 imaging from continuous non-gated acquisitions. *Magn. Reson. Med.* 84, 609 1763–1780. doi:[10.1002/mrm.28235](https://doi.org/10.1002/mrm.28235).
- 610 Pipe, J.G., Farthing, V.G., Forbes, K.P., 2002. Multishot diffusion-weighted 611 FSE using PROPELLER MRI. *Magn. Reson. Med.* 47, 42–52. doi:[10.1002/mrm.10014](https://doi.org/10.1002/mrm.10014).

- 613 Polak, D., Splitthoff, D.N., Clifford, B., Lo, W.C., Huang, S.Y., Conklin, J.,
614 Wald, L.L., Setsompop, K., Cauley, S., 2022. Scout accelerated motion
615 estimation and reduction (SAMER). Magn. Reson. Med. 87, 163–178.
616 doi:[10.1002/mrm.28971](https://doi.org/10.1002/mrm.28971).
- 617 Porter, D.A., Heidemann, R.M., 2009. High resolution diffusion-weighted
618 imaging using readout-segmented echo-planar imaging, parallel imaging
619 and a two-dimensional navigator-based reacquisition. Magn. Reson. Med.
620 62, 468–475. doi:[10.1002/mrm.22024](https://doi.org/10.1002/mrm.22024).
- 621 Pruessmann, K.P., Weiger, M., Scheidegger, M.B., Boesiger, P., 1999.
622 SENSE: Sensitivity encoding for fast MRI. Magn. Reson. Med. 42, 952–
623 962. doi:[10.1002/\(SICI\)1522-2594\(199911\)42:5<952::AID-MRM16>3.0.CO;2-S](https://doi.org/10.1002/(SICI)1522-2594(199911)42:5<952::AID-MRM16>3.0.CO;2-S).
- 625 Ra, J.B., Rim, C.Y., 1993. Fast imaging using subencoding data sets from
626 multiple detectors. Magn. Reson. Med. 30, 142–145. doi:[10.1002/mrm.1910300123](https://doi.org/10.1002/mrm.1910300123).
- 628 Roemer, P.B., Edelstein, W.A., Hayes, C.E., Souza, S.P., Mueller, O.M.,
629 1990. The NMR phased array. Magn. Reson. Med. 16, 192–225. doi:[10.1002/mrm.1910160203](https://doi.org/10.1002/mrm.1910160203).
- 631 Setsompop, K., Fan, Q., Stockmann, J., Bilgic, B., Huang, S., Cauley, S.F.,
632 Nummenmaa, A., Wang, F., Rathi, Y., Witzel, T., Wald, L.L., 2018. High-
633 resolution *in vivo* diffusion imaging of the human brain with generalized
634 slice dithered enhanced resolution: Simultaneous multislice (gSlider-SMS).
635 Magn. Reson. Med. 79, 141–151. doi:[10.1002/mrm.26653](https://doi.org/10.1002/mrm.26653).

- 636 Setsompop, K., Gagoski, B.A., Polimeni, J.R., Witzel, T., Wedeen, V.J.,
637 Wald, L.L., 2012. Blipped-controlled aliasing in parallel imaging for si-
638 multaneous multislice echo planar imaging with reduced *g*-factor penalty.
639 Magn. Reson. Med. 67, 1210–1224. doi:[10.1002/mrm.23097](https://doi.org/10.1002/mrm.23097).
- 640 Shafieizargar, B., Jeurissen, B., Poot, D.H.J., Klein, S., Van Audekerke,
641 J., Verhoye, M., den Dekker, A.J., Sijbers, J., 2023. ADEPT: Accurate
642 diffusion echo-planar imaging with multi-contrast shoTs. Magn. Reson.
643 Med. 89, 396–410. doi:[10.1002/mrm.29398](https://doi.org/10.1002/mrm.29398).
- 644 Tournier, J.D., Smith, R., Raffelt, D., Tabbara, R., Dhollander, T., Pietsch,
645 M., Christiaens, D., Jeurissen, B., Yeh, C.H., Connelly, A., 2019. MRtrix3:
646 A fast, flexible and open software framework for medical image processing
647 and visualisation. NeuroImage 202, 116137. doi:<https://doi.org/10.1016/j.neuroimage.2019.116137>.
- 648 Trzasko, J., Manduca, A., 2011. Local versus global low-rank promotion in
649 dynamic MRI series reconstruction, in: Proceedings of the 19th Annual
650 Meeting of ISMRM, Montréal, CAN, p. 4371.
- 652 Tuch, D.S., Reese, T.G., Wiegell, M.R., Makris, N., Belliveau, J.W., Wedeen,
653 V.J., 2002. High angular resolution diffusion imaging reveals intravoxel
654 white matter fiber heterogeneity. Magn. Reson. Med. 48, 577–582. doi:[10.1002/mrm.10268](https://doi.org/10.1002/mrm.10268).
- 656 Uecker, M., Lai, P., Murphy, M.J., Virtue, P., Elad, M., Pauly, J.M.,
657 Vasanawala, S.S., Lustig, M., 2014. ESPIRiT – an eigenvalue approach

- 658 to autocalibrating parallel MRI: Where SENSE meets GRAPPA. Magn.
659 Reson. Med. 71, 990–1001. doi:[10.1002/mrm.24751](https://doi.org/10.1002/mrm.24751).
- 660 Wu, W., Koopmans, P.J., Andersson, J.L., Miller, K.L., 2019. Diffusion
661 Acceleration with Gaussian process Estimated Reconstruction (DAGER).
662 Magn. Reson. Med. 82, 107–125. doi:[10.1002/mrm.27699](https://doi.org/10.1002/mrm.27699).
- 663 Wu, W., Miller, K.L., 2017. Image formation in diffusion MRI: A review
664 of recent technical developments. J. Magn. Reson. Imaging 46, 646–662.
665 doi:[10.1002/jmri.25664](https://doi.org/10.1002/jmri.25664).
- 666 Zhang, T., Pauly, J.M., Levesque, I.R., 2015. Accelerated parameter mapping
667 with a locally low rank constraint. Magn. Reson. Med. 73, 655–661. doi:[10.1002/mrm.25161](https://doi.org/10.1002/mrm.25161).